# Isolobal Analogies in Intermetallics: The Reversed Approximation MO Approach and Applications to CrGa₄- and Ir₃Ge₇-Type Phases

Vincent J. Yannello, Brandon J. Kilduff, and Daniel C. Fredrickson*

Department of Chemistry, University of Wisconsin-Madison, 1101 University Avenue, Madison, WI 53706, United States

Ⓢ *Supporting Information*

ABSTRACT: Intermetallic phases offer a wealth of unique and unexplained structural features, which pose exciting challenges for the development of new bonding concepts. In this article, we present a straightforward approach to rapidly building bonding descriptions of such compounds: the reversed approximation Molecular Orbital (raMO) method. In this approach, we reverse the usual technique of using linear combinations of simple functions to approximate true wave functions and employ the fully occupied crystal orbitals of a compound as a basis set for the determination of the eigenfunctions of a simple, chemically transparent model Hamiltonian. The solutions fall into two sets: (1) a series of functions representing the best-possible approximations to the model system's eigenstates constructible from the occupied crystal orbitals and (2) a second series of functions that are orthogonal to the bonding picture represented by the model Hamiltonian. The electronic structure of a compound is thus quickly resolved into a series of orthogonal bonding subsystems. We first demonstrate the raMO analysis on a familiar molecule, 1,3-butadiene, and then move to illustrating its use in discovering new bonding phenomena through applications to three intermetallic phases: the PtHg₄-type CrGa₄ and the Ir₃Ge₇-type compounds Os₃Sn₇ and Ir₃Sn₇. For CrGa₄, a density of states (DOS) minimum coinciding with its Fermi energy is traced to 18-electron configurations on the Cr atoms. For Os₃Sn₇ and Ir₃Sn₇, 18-electron configurations also underlie DOS pseudogaps. This time, however, the 18-electron counts involve multicenter interactions isolobal with classical Ir–Ir or Os–Os covalent bonds, as well as Sn–Sn single bonds serving as electron reservoirs. Our results are based on DFT-calibrated Hückel calculations, but in principle the raMO analysis can be implemented in any method employing one-electron wave functions.
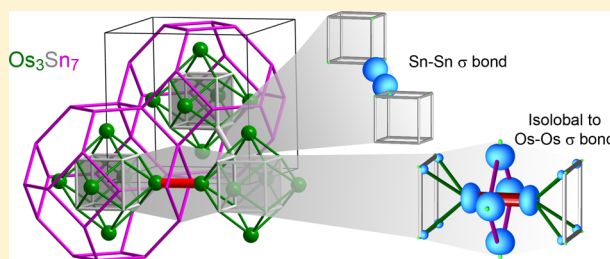
1. INTRODUCTION

From the dense atomic packing and large coordination numbers present in intermetallic phases, one might expect that their chemical bonding may be more akin with that of simple metals and alloys than with that of molecular systems. And yet, there are alluring hints that the same language of orbital interactions that has been transformative for molecular chemistry may be used (though in a hitherto unknown dialect) in these compounds. Most important of these clues is perhaps the correlation of phase stability with the presence of a band gap or pseudogap near the Fermi energy (E_F) separating filled and empty electronic levels.[1−23] Much as the size of a HOMO−LUMO gap in a molecule is an indicator of its stability and reactivity, the width and depth of an intermetallic's gap at the E_F largely governs its formation and potential physical properties, such as electrical conductivity, magnetic phenomena, and thermoelectric effects.[24] The connection with molecular systems is strengthened by the realization that these electronic features are reproducible with simple orbital-based models, such as the simple and extended Hückel methods.[25,26] However, distilling the results of these calculations into bonding schemes with utility for materials design remains a challenge.

The greatest progress in explaining the presence of pseudogaps in terms of chemical bonding has been made in certain limiting cases of intermetallics. The Zintl phases, such as NaTl, represent the extreme of high bond polarity in compounds formed between metallic elements.[27−33] For these compounds, closed-shell electron configurations are obtained on the atoms via formal electron transfer from the electropositive to the electronegative element and the covalent sharing of electrons. Electron counts corresponding to the filling of these closed shells are often correlated with pseudogaps at the Fermi energy. At another extreme are phases well-described by the nearly free electron model, where delocalization of the electrons is so complete that they are only weakly perturbed by the ion cores they surround. For these compounds, pseudogaps can be traced to the intersection of the Fermi surface with the Brillouin zone boundary.[1−3]

The predominance of pseudogaps is no less pronounced for other intermetallics, but rationales for explaining and predicting their positions in the electronic density of states (DOS) distributions are still needed. For example, gap/pseudogap formation in transition metal (T)−main group (E) phases is

commonly attributed to interactions between the T d and the E p or sp orbitals,[6−10] but still unknown is how these interactions conspire with the crystal structures to place gaps at specific electron counts. Recently, there have been hints of a more detailed bonding scheme from theoretical work on the half-Heusler phases and other derivatives of the fluorite structure type.[14−18] For each of these compounds, pseudogaps at the E_F can be connected to the filling of molecular orbital (MO) diagrams centered on the T atoms that are nearly isolobal with those of molecular 18-electron complexes.

This success suggested to us that the isolobal analogy might elucidate the preferred electron counts of other intermetallic structures and offer general electron-counting rules for this family of compounds. In this article, we present a theoretical method examining the electronic structures of intermetallics in terms of such analogies to simple MO schemes: the reversed approximation Molecular Orbital (raMO) analysis. Our approach here is motivated by ways in which vast improvements in computational power and methodology have changed the nature of the approximations needed for chemical theory. The original approximations employed in MO calculations, such as the representation of the full wave function with a linear combination of atomic orbitals (LCAO) basis set, served to simplify the process of solving the electronic structure of a molecule. Now that computational power is no longer a limiting factor in many cases, the challenge has shifted toward interpreting the wealth of information provided by a calculation in terms of a chemically meaningful picture. In other words, *interpretative* rather than *numerical* approximations are becoming increasingly needed. This issue is particularly pressing for intermetallics, where few bonding models are available to serve as a cipher for the decoding of computational output.

In the raMO approach, we reverse the usual basis set approximation of MO calculations to fill this need: we use the fully occupied wave functions of a system as an approximate basis set for the solution of a simple chemical problem, such as the interactions between ligand σ orbitals and a transition metal atom. Solving the Schrödinger equation for this model system in this basis then results in two sets of functions: (1) those with nonzero eigenvalues that provide the approximation to the true eigenstates of the model system possible from linear combinations of the full compound's occupied orbitals and (2) those with eigenvalues of 0, which are orthogonal to the bonding picture represented by the model system. In this way the molecular or crystal orbitals of a compound can be transformed into orthogonal bonding systems.

Formally, the raMO analysis is a procedure for the creation of localized molecular orbitals[34] or Wannier functions.[35−39] Its distinctness among other types of Wannier analyses lies in its goal of forging isolobal analogies.[40] Rather than seeking out linear combinations of occupied wave functions with specific spatial properties (e.g., maximal localization), the raMO analysis maps these wave functions onto simple, familiar molecular orbital diagrams.[41] In its apportioning of electrons to recognizable bonding systems, the method is more closely aligned with the powerful Natural Bond Orbital (NBO) analysis[42] but is specifically designed to handle the delocalized character of metals.[43]

Over a series of examples in this article (Figure 1), we will see that the raMO approach allows for the rapid deconstructions of the electronic structures of intermetallics into chemically familiar bonding schemes. In this way, the method offers a means of addressing the ever-widening gap between the
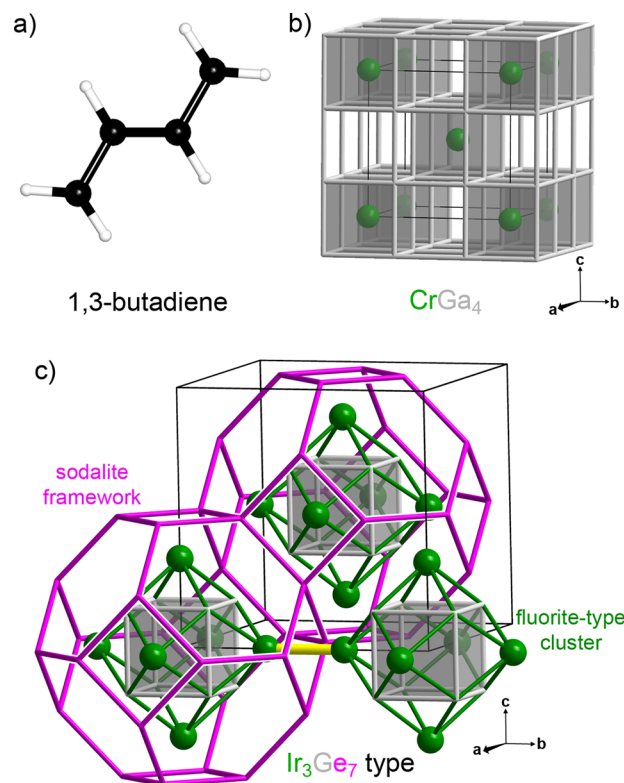

Figure 1. Compounds whose bonding will be investigated using the reverse approximation molecular orbital (raMO) method in this article: (a) 1,3-butadiene; (b) the PtHg$_4$-type phase CrGa$_4$; (c) Ir$_3$Ge$_7$-type phases.

discovery of new structural phenomena in inorganic materials and their explanation in terms of experimentally useful bonding concepts.

2. TECHNICAL PROCEDURES

To provide a basis for the parametrization of simple Hückel models for the compounds discussed in this work, the DFT band energies and electronic DOS distributions were calculated for the crystal structures of benzene (as a representative of conjugated hydrocarbons, including 1,3-butadiene),[44] CrGa$_4$,[45] Os$_3$Sn$_7$,[46] and Ir$_3$Sn$_7$[47] using the Vienna ab initio simulation package (VASP).[48,49] All calculations were performed in the high-precision mode, using the LDA ultrasoft pseudopotentials[50] provided with the package. Further details such as the energy cutoffs and k-point grids used are given in the Supporting Information.

The output of each VASP calculation was then used as a reference for the refinement of Hückel parameters using the program eHtuner,[51] with the actual Hückel calculations being carried out with YAeHMOP.[52] The optimized Hückel parameters are tabulated in the Supporting Information, along with the root-mean-squared deviations between the band energies of the Hückel models and those calculated with VASP (typically <0.25 eV).

Once the Hückel parametrization for each compound was complete, a Hückel calculation was carried out using a 2 × 2 × 2 supercell, so that several of the special k points of the primitive cell became mapped to the Γ point. The Hamiltonian matrix for the Γ point of this supercell was then printed and imported into MATLAB for processing as described below.

3. THE REVERSED APPROXIMATION MO APPROACH

3.1. The raMO Procedure. As with most other modern theoretical methods for analyzing bonding, our goal is to interpret the solutions of the Schrödinger equation

$$\hat{H}|\psi_j\rangle = E_j|\psi_j\rangle \qquad (1)$$

in terms of familiar chemical interactions. For intermetallic phases, the wave functions that result from, for example, a DFT calculation are numerous and complicated. Often they spread across the whole lattice of the crystal and are organized in k space rather than by their properties in physical space. In this section, we will describe the raMO approach for extracting simple MO interaction schemes from these complex electronic structures. To demonstrate the steps of the procedure, we will make use of a well-understood molecular system, 1,3-butadiene (Figure 1a), considering the question of how independent the π bonds in its Lewis structure are from each other.

We begin with the assumption that in the full set of interacting orbitals for a system, a subset interacts in a fashion that is analogous to a well-understood molecular system. For this subsystem, we have a simplified Schrödinger equation:

$$\hat{H}^{\circ}|\psi_k^{\circ}\rangle = E_k^{\circ}|\psi_k^{\circ}\rangle \qquad (2)$$

where $\hat{H}^{\circ}$ is the Hamiltonian operator within this subspace and its eigenstates are given by $|\psi_k^{\circ}\rangle$. In the case of 1,3-butadiene, we might consider one of the two π bonds drawn in the standard Lewis structure (Figure 2), each of which is individually more simple than the full conjugated π system: the eigenfunctions resulting from the π interaction between two C 2p orbitals are just an in-phase π bonding orbital and an out-of-phase π^* orbital (Figure 2a).

We now look to the question of how well the $|\psi_k^{\circ}\rangle$ states are represented by linear combinations of the occupied eigenstates of the full system, i.e. to what degree the following equation is satisfied:

$$|\psi_k^{\circ}\rangle \approx \sum_j c_j|\psi_j\rangle, \quad j = \text{occupied states} \qquad (3)$$

The degree to which such expressions are fulfilled measures the validity of the proposed analogy between a model MO diagram and the electronics of the full compound. The form of the expression bears a resemblance to the equation representing the linear combination of atomic orbitals (LCAO) approximation, as both use a limited basis set to reconstruct a target function. In the case of LCAO, one determines the best approximation of the true ground state wave function by minimizing the energy with respect to the atomic orbital coefficients.

Here, we perform a similar procedure to obtain the best approximations to the model orbitals from the full wave functions. We first write out the model Hamiltonian in terms of its eigenfunctions, recalling that the eigenfunctions of a quantum mechanical operator comprise a complete set:[53]

$$\hat{H}^{\circ} = \hat{H}^{\circ}\cdot 1 = \hat{H}^{\circ}\left(\sum_k |\psi_k^{\circ}\rangle\langle\psi_k^{\circ}|\right) = \sum_k |\psi_k^{\circ}\rangle E_k^{\circ}\langle\psi_k^{\circ}| \qquad (4)$$

In our example of a two-center π bond in 1,3-butadiene, this operator has two terms (Figure 2a, right). One term projects the function it acts upon onto a C−C π bonding orbital with a weight of the energy of this orbital. The other term carries out the analogous projection of the function onto a C−C π^* orbital.
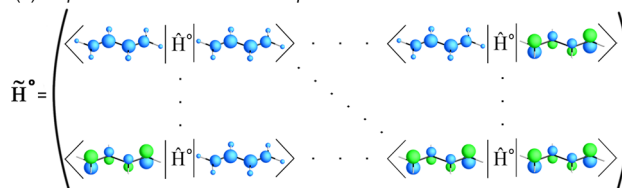
Next, we calculate model Hamiltonian matrix elements in the basis of the occupied wave functions of the full system:

raMO analysis of π-bond in 1,3-butadiene

(a) Step 1. Construct Hamiltonian for model orbital system ($\hat{H}^{\circ}$).
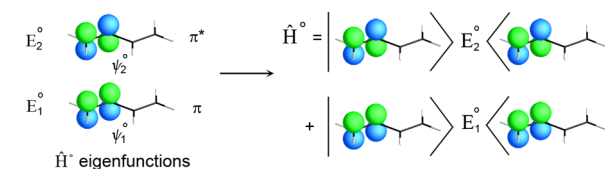
(b) Step 2. Write $\hat{H}^{\circ}$ in basis of occupied MOs of full molecule.

(c) Step 3. Diagonalize $\tilde{\mathbf{H}}^{\circ}$ to obtain approximate eigenfunctions $\{\tilde{\psi}^{\circ}\}$ for bonding analysis.

$\langle E^{\circ}\rangle \neq 0$: best approximations to ψ_1°, ψ_2°

$\langle E^{\circ}\rangle = 0$: orthogonal $\tilde{\psi}_n^{\circ}$'s belonging to other bonding subsystems

$\tilde{\psi}_2^{\circ}$ $P_{target} = 0.03$ $P_{fragment} = 1.00$

$\tilde{\psi}_1^{\circ}$ $P_{target} = 0.97$ $P_{fragment} = 1.00$

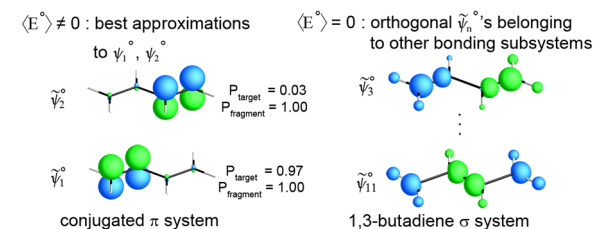conjugated π system   1,3-butadiene σ system

Figure 2. The raMO procedure illustrated with the analysis of a π bond in 1,3-butadiene. (a) Step 1: the eigenfunctions of a simplified orbital system are used to construct a model Hamiltonian operator, $\hat{H}^{\circ}$. (b) Step 2: this $\hat{H}^{\circ}$ operator is expressed in terms of matrix elements between the occupied MOs of the full molecule, to give the $\tilde{\mathbf{H}}^{\circ}$ matrix. (c) Step 3: diagonalization of the $\tilde{\mathbf{H}}^{\circ}$ matrix yields an orthonormal set of linear combinations of the occupied MOs which divides naturally into two classes. Those with nonzero expectation values, $\langle E^{\circ}\rangle$, of $\hat{H}^{\circ}$ represent the best possible approximations to the original eigenfunctions of the model, while those with $\langle E^{\circ}\rangle = 0$ belong to separate bonding subsystems in the compound.

$$\tilde{H}_{ij}^{\circ} = \langle\psi_i|\left(\sum_k |\psi_k^{\circ}\rangle E_k^{\circ}\langle\psi_k^{\circ}|\right)|\psi_j\rangle = \sum_k E_k^{\circ}\langle\psi_i|\psi_k^{\circ}\rangle\langle\psi_k^{\circ}|\psi_j\rangle \qquad (5)$$

Here, the tilde above the matrix element symbol indicates that it is part of an approximate matrix representation of the operator in eq 4, built from the incomplete basis set (the occupied wave functions). As is illustrated in Figure 2b, the construction of this matrix for 1,3-butadiene would involve all of the occupied MOs of both the σ system and the conjugated π system. In principle, these MOs could be taken from the results of Hartree−Fock, DFT, or other methods employing one-electron wave functions. For simplicity, here we use MOs obtained from a DFT-calibrated simple Hückel calculation.

Once the matrix elements of $\tilde{\mathbf{H}}^{\circ}$ are obtained, the procedure is completed by the diagonalization of the $\tilde{\mathbf{H}}^{\circ}$ matrix to yield eigenvectors and eigenvalues. The eigenvectors form an orthonormal set of functions $\{\tilde{\psi}_k^{\circ}\}$ that are organized by their eigenvalues according to their relationships to a model bonding system. Those with eigenvalues not equal to zero ($\langle\tilde{E}^{\circ}\rangle \neq 0$) represent the optimal fit between the MOs of our simple model system and occupied wave functions of the full Hückel calculation. The remaining functions with eigenvalues of 0

($\langle E^{\circ} \rangle = 0$) build up a series of functions that are orthogonal to the model system. This set consists of linear combinations of the occupied wave functions that contribute to other bonding subsystems of the molecule.

The results of this final step for a π bond in 1,3-butadiene illustrate the information obtainable from this procedure (Figure 2c). Two eigenvectors with $\langle \tilde{E}^{\circ} \rangle \neq 0$ are obtained, $\tilde{\psi}_1^{\circ}$ and $\tilde{\psi}_2^{\circ}$. The first represents the best approximation to the π-bonding orbital between carbon atoms 1 and 2 (C1 and C2) possible from the occupied levels (while maintaining orthogonality to the other eigenvectors). The second shows the best attempt at reconstructing an π^* orbital between those atoms. Not surprisingly, given the strong π bonding present in this molecule, the π-bonding orbital is well-reconstructed in $\tilde{\psi}_1^{\circ}$, while very little of the true π^* orbital appears in $\tilde{\psi}_2^{\circ}$.

More insight can be obtained into the bonding in the 1,3-butadiene π system by looking more closely at the forms of these functions. $\tilde{\psi}_1^{\circ}$ is predominantly based on a π bond between C1 and C2, but small contributions can also be seen on C3 and C4. These appear as a miniature C3−C4 π^* orbital, with bonding overlap occurring between C2 and C3 at the center of the molecule. This function altogether then represents a C1−C2 π bond that is donating electron density to the π^* orbital of the C3−C4 interaction, in a Lewis acid/base fashion. The $\tilde{\psi}_2^{\circ}$ function can be interpreted in a similar fashion, but this time we see that the C1−C2 π^* function that we intended to create through the raMO analysis exists only by virtue of its receiving electron density through its bonding overlap with a C3−C4 π bond.

The large mismatch in relative contributions between the π bonding and π antibonding components of these functions indicates that to a large extent the bonding in the π system can be viewed as a perturbation on separate C1−C2 and C3−C4 π bonds. The conjugation we associate with this system then appears from this localized view in the partial donation of their electron pairs into the π^* orbitals of their neighbor, a view which converges with the donor−acceptor picture for conjugation that emerges from a NBO analysis.[42] This is, in fact, just another way of viewing the full MOs of the 1,3-butadiene π system: in adding and subtracting $\tilde{\psi}_1^{\circ}$ and $\tilde{\psi}_2^{\circ}$, we can recover the molecule's occupied π MOs.

The remaining eigenvectors of the $\tilde{\mathbf{H}}^{\circ}$ matrix have eigenvalues of 0 and form as series of functions that have no overlap with the π and π^* orbitals of our model MO diagram. Nine of these functions are obtained (Figure 2c, right), which represent the bonding orbitals of the σ framework of the molecule.

So far, we have only considered the occupied MOs of the 1,3-butadiene. In predicting the reactivity of a molecule, one should also consider the low-lying unoccupied MOs as well. This can be accomplished in the raMO framework by using the unoccupied one-electron wave functions as a basis for the eigenfunctions of the model Hamiltonian operator. The results of this process for a π bond in 1,3-butadiene are shown in Figure 3. In this case, the reverse of the situation in Figure 2c is obtained: the π^* function on each the terminal pair of C atoms is destabilized by an antibonding interaction with the π-bonding function on the neighboring pair.

Using the example of 1,3-butadiene, we have seen the potential for the raMO analysis to quickly dissect the electronic structure of a compound. By starting with a simple test of the degree of π bonding between two carbon atoms, we immediately obtained the conjugated π system (in a localized
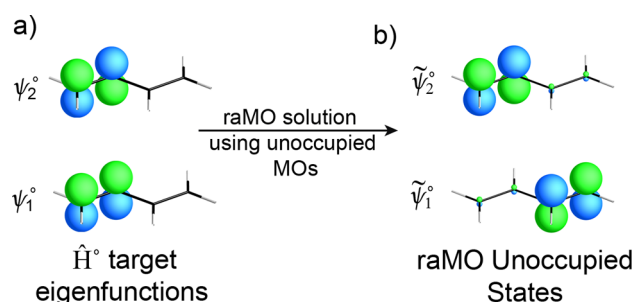

Figure 3. raMO reconstruction of the bonding and antibonding functions of a π bond using the unoccupied MOs of 1,3-butadiene: (a) the target eigenfunctions; (b) the best approximants to the target eigenfunctions built from the unoccupied MOs.

form) and the orthogonal σ system. While this largely reiterates familiar themes in the bonding of organic molecules, we will see soon how similarly intuitive bonding schemes can be constructed for much more complicated chemical systems, namely intermetallic phases.

3.2. Quantitative Analysis of raMO Results. In our raMO analysis of the π system of 1,3-butadiene, we found that for either of the localized π bonds in the standard Lewis structure there is some occupation of both the bonding and antibonding orbitals. As we move to less familiar systems, it will be helpful to have ways of quantifying the relative occupations of such bonding/antibonding pairs. One tool for doing this is to calculate the projection of the target eigenfunction onto its corresponding raMO approximant: $\langle \tilde{\psi}_n^{\circ} | \psi_n^{\circ} \rangle$. In particular, the square of this projection, is simply the probability that an electron in the raMO function would be found in the target eigenstate if it were interrogated with the proper measurement. We term this probability as $P_{target} = |\langle \tilde{\psi}_n^{\circ} | \psi_n^{\circ} \rangle|^2$, which serves as a measure of how well the target eigenstate is represented in the occupied wave functions of the system.

The P_{target} values of π bonding and antibonding target eigenstates are given alongside their raMO approximants in Figure 2. The P_{target} value for the π bonding function is 0.97, which indicates a 97% probability of finding that π bond occupied. The corresponding probability for the π antibonding function is only 3%, which agrees well with the 3.65% value obtained from an earlier NBO analysis.[42]

In the periodic structures that we will be discussing in the remainder of the article, it will become impractical to show the raMO functions in the context of the full crystal structure. Instead, we will focus on local features of interest for our discussion of bonding. For this reason, it is useful to introduce another quantity, $P_{fragment}$, which gives the probability of finding an electron in a raMO function in the fragment of the structure portrayed in the figure. In the case of 1,3-butadiene, the full molecule is shown for all of the raMOs in Figure 2. As such, $P_{fragment} = 1$ throughout. For the other structures in this paper, the $P_{fragment}$ values will provide a measure of how much the electron density of a raMO function spills out of the region displayed.

4. CrGa$_4$ AS AN 18-ELECTRON COMPOUND

Having illustrated how the raMO method works using a well-understood molecular system, we are now in a position to see what it can tell us about the more elusive interactions underlying the stability of intermetallic phases. Let us begin with a simple example for which theoretical calculations

indicate that electron count plays a central role: the PtHg$_4$-type phase CrGa$_4$ (Figure 4). In this compound, the Ga atoms form a primitive cubic array (gray), with the Cr atoms (green) lying at the centers of one-fourth of the cubic voids. The Cr@Ga$_8$ cubic polyhedra are arranged so that the full structure can be viewed as a body-centered cubic lattice of these polyhedra linked through vertex sharing.
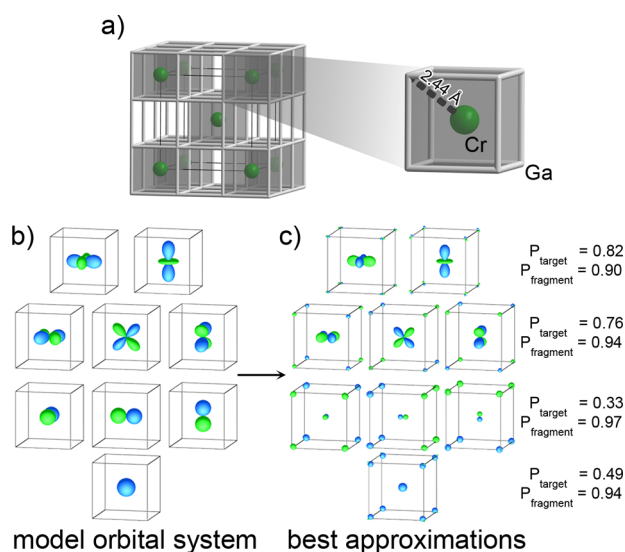

Figure 4. raMO analysis revealing CrGa$_4$ to be an 18-electron compound: (a) the crystal structure of CrGa$_4$, with the Cr atoms' cubic coordination by Ga highlighted (Cr, green; Ga, gray); (b) the basis of Cr 4s, 3d, and 4p orbitals used as the model MO system for the raMO analysis; (c) the nine reconstructed functions resulting from the raMO analysis, corresponding to Cr–Ga bonding and Cr nonbonding orbitals localized around the original Cr atom. Each function is calculated to have an energy lying below the E_F of the compound. Together they form a complete 18-electron configuration on the Cr atom.

This structure's partial filling of a primitive cubic network of main group atoms by transition metals is mirrored in a number of compounds: the half-Heusler phases and fluorite-type silicides such as NiSi$_2$. In all of these compounds, a pseudogap appears in the electronic DOS distributions corresponding to 18-electron configurations on the TM atoms.[13−17,54,55] CrGa$_4$ adheres to this special electron count ($9 \times 1 + 3 \times 3 = 18$), and its electronic DOS distribution has been calculated to exhibit the expected deep minimum at the Fermi energy (E_F) lying just above a dense series of states based on Cr 3d orbitals.[9] For the other compounds in this family, the favorability of the 18-electron count is traced to the involvement of all of the TM d, s, and p valence orbitals of the atoms, as in a molecular transition metal complex. The raMO approach allows us to quickly test this hypothesis for CrGa$_4$.

In this interpretation of the 18-electron count, the occupied orbitals of the system should be expressible as localized functions with a 1:1 correspondence with the d, s, and p orbitals of the TM atoms. The corresponding model Hamiltonian operator ($\hat{H}^\circ$) expressing this assumption could then be written using the atomic valence orbitals of a TM atom as $|\psi_k^\circ\rangle$'s (Figure 4b). This operator can then be used, following the procedure outlined in Figure 2, to analyze the wave functions obtained from a band structure calculation on the CrGa$_4$ crystal structure.

To obtain the wave functions for the full structure, we parametrized a simple Hückel model for CrGa$_4$, using our program *eHtuner*,[51] against the band energies and projected DOS curves calculated with GGA-DFT (see Technical Procedures for further details). The reasonable correspondence obtained (RMS deviation in the band energies ca. 0.1 eV) allows us to use our Hückel model as a guide to interpreting the DFT results. We then performed a periodic Hückel calculation using a $2 \times 2 \times 2$ supercell of the conventional CrGa$_4$ unit cell so that multiple k points in the Brillouin zone are mapped to the Γ point.[25,26] The wave functions and Hamiltonian matrix for Γ were then output and considered as representative of the interactions of the system.

Upon writing the $\hat{H}^\circ$ operator in terms of the basis of occupied wavefunctions (step 2) and diagonalizing the resulting matrix (step 3), we obtain nine functions with non-zero eigenvalues. These are shown in Figure 4c, where it can be seen that one function appears for each of the TM s, p, and d orbitals. The s and p orbital based functions are augmented by bonding interactions with Ga σ orbitals (appearing in the appropriate symmetry-adapted linear combinations). The t_{2g} 3d orbitals partake in similar Cr–Ga bonding interactions, while the e_g orbitals are essentially nonbonding, with only very minor π type contributions from the Ga. All of these functions shows only small components beyond the first-coordination environment of the central Cr atom ($P_{\text{fragment}} \approx 1.0$), indicating that they can be assigned entirely to this Cr site. No interactions between Cr atoms are apparent.

These results support the view that the 18-electron count in the CrGa$_4$ structure is associated with each of the Cr's valence orbitals being utilized. As this would account for all valence electrons in the phase, we should be able to build a $\hat{H}^\circ$ operator that accounts for the full electronic structure of the compound using the s, p, and d orbitals of all Cr atoms as $|\psi_k^\circ\rangle$'s. Carrying out such a raMO analysis leads to no eigenfunctions with eigenvalues of 0, indicating that there are no additional bonding subsystems at work in the compound. From this point of view, we would then expect that the band structure of CrGa$_4$ would be fully interpretable in terms of weakly interacting Cr octadecets.

The features of the electronic density of states (DOS) distribution of CrGa$_4$ can be understood in this way (Figure 5). The DOS curve begins at low energies with a somewhat parabolic shape. Such low-energy tails are often interpreted as sp nearly free-electron levels,[56] which is consistent with the large absence of Cr d character (shaded portion of distribution) seen in this region. This sp distribution is interrupted at ca. −8.5 eV by a sharp peak of Cr d-rich states. Above this peak lies the Fermi energy (E_F) in a deep DOS minimum, followed by a dense series of unoccupied levels.

Alongside the DOS curve, we also plot the energy expectation values calculated for the nine $\tilde{\psi}_n^\circ$ values resulting from the raMO analysis of CrGa$_4$. The four lowest-energy functions correspond to the Cr 4s and 4p orbitals, with significant bonding contributions from sp hybrid orbitals on the surrounding Ga atoms. As these functions are derived primarily from s and p orbitals, it is fitting that their energies are aligned with the middle of the low-energy DOS features arising from the nearly free electron sp states. The wide energy range of the sp DOS distribution is then viewed as stemming from the broadening of the energies of raMO sp functions upon their inclusion in their context of the full crystal structure.
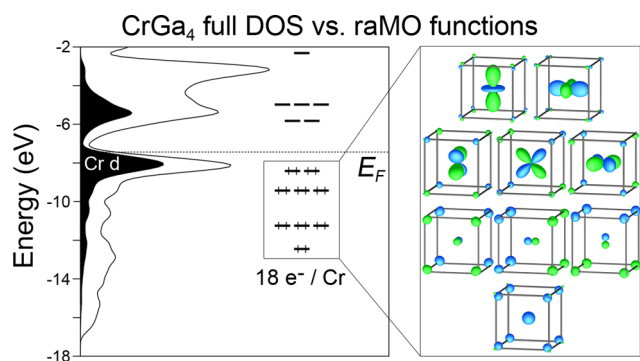
Figure 5. Comparison of the GGA-DFT DOS distribution calculated for $CrGa_4$ with energies of the Cr 3d-based functions obtained from a raMO analysis of the occupied bands of a DFT-calibrated Hückel calculation on $CrGa_4$. In the energy level diagram, the levels drawn above the E_F are derived from a raMO analysis of the unoccupied bands. Contributions to the total DOS from the Cr d are shaded. The DOS curve has been treated with Gaussian broadening to make its general features more apparent.

The remaining five raMO functions are dominated by the original Cr 3d orbitals, which are split in energy according to whether they are Cr–Ga bonding (t_{2g}) or nonbonding (e_g). As is anticipated by their nonbonding character, the e_g functions are coincident in energy with the sharp DOS peak of Cr 3d states. The t_{2g} functions experience stronger interactions with the Ga sp and as such correspond in energy with the top of a lower energy tail in the Cr 3d DOS contribution which stretches downward into the total DOS curve's sp region.

Filling all of these raMO states brings the HOMO level for this diagram to just under the E_F and DOS minimum of the compound's DOS curve. The pseudogap can thus be seen as consistent with the filling of 18-electron configurations on the Cr atoms. In this way, the raMO method gives an estimate of the lower boundary of the pseudogap region.

So far, however, the raMO approach has not provided any information on where the pseudogap region should end: i.e., where the lowest unoccupied molecular orbital (LUMO) levels for our simple MO model for $CrGa_4$ should lie. To investigate the character of the unfilled levels of the DOS distribution, we can repeat the steps of the raMO analysis (as shown schematically in Figure 2), but this time using the unoccupied crystal orbitals as our basis set. The resulting energy levels appear in Figure 4 above the E_F of $CrGa_4$. They coincide closely with the dense block of states in the DOS appearing above the pseudogap. The energy difference between the lowest of these functions (which might be termed the raMO LUMO) and the highest of the original raMO functions (the raMO HOMO) straddles the full compound's DOS pseudogap.

In this section, we have seen how the raMO approach provides a simple means of interpreting the electronic structure of $CrGa_4$. Its DOS pseudogap at the E_F arises from a filling of 18-electron configurations on the Cr atoms. Some of these Cr-based levels experience significant energy broadening through their bonding interactions with the Ga sp. However, in terms of bookkeeping, every electron can be associated with a valence orbital on the Cr.

5. ELECTRON COUNTING IN THE Ir_3Ge_7 TYPE

Let us now move to more complicated compounds in which a simple assignment of 18-electron configurations is not sufficient for rationalizing the bonding: the Ir_3Ge_7-type phases (Figure

1c). This structure is observed for a rather large range of electron counts (17–18.67 electrons/transition metal atom), which we will sample with Os_3Sn_7 (17.3 electrons/Os) and Ir_3Sn_7 (18.3 electrons/Ir). The higher end of this electron count range is in excess of 18, suggesting the availability of states for accepting electrons beyond transition metal-based bonding and nonbonding orbitals. Meanwhile, the lower range falls short of a complete octadecet for individual transition metal atoms, and one might anticipate covalent sharing of electrons between transition metal atoms as a way of responding to this deficiency. As we will see in this section, both of these pictures are relevant to bonding in the Ir_3Ge_7 type.

We begin with the possibility of Os–Os bonding electron pairs in Os_3Sn_7. Hints of such Os–Os interactions can be seen in the crystal structure of this phase (Figure 6a). The structure
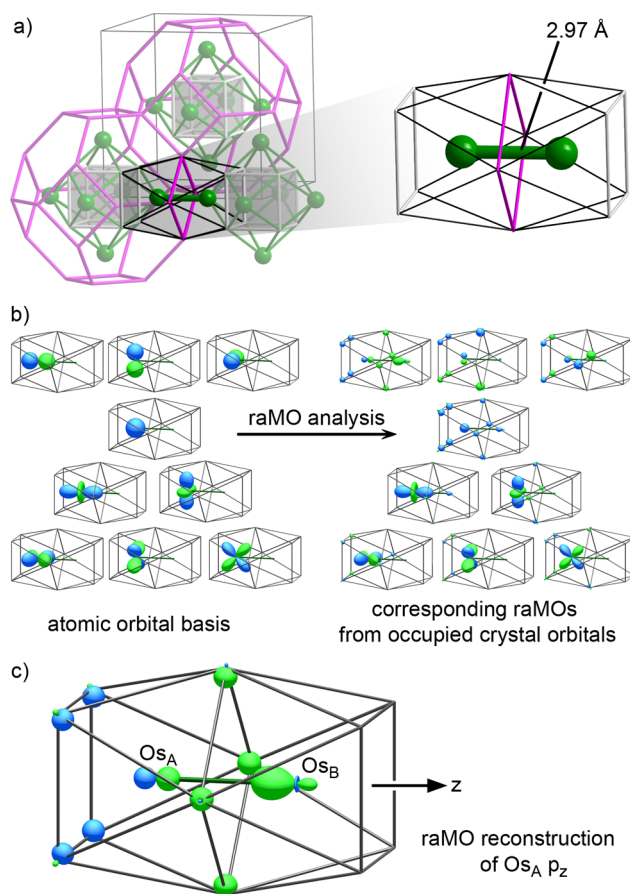

Figure 6. raMO analysis of the Ir_3Ge_7-type Os_3Sn_7, using the 5d, 6s, and 6p orbitals of a single Os atom as target eigenstates: (a) the crystal structure of Os_3Sn_7, with one of the Os dimers that link its fluorite-type fragments highlighted; (b) the target eigenstates, and their best approximant raMOs obtained from the occupied crystal orbitals of Os_3Sn_7; (c) magnified view of the Os–Os σ-bonding function that emerges in the generation of the raMOs.

is based on a body-centered packing of small fragments of the fluorite structure type (as is adopted by the related compounds $CoSi_2$ and $NiSi_2$). Each fragment consists of an empty Sn_8 cube, with an Os atom capping each of its square faces. The fragments are placed in the void spaces of a sodalite-type network of Sn atoms (face-sharing truncated octahedra). Through the shared square faces of the Sn sodalite cages

(purple), the Os atoms from neighboring fluorite-type clusters meet with a contact distance of 2.97 Å (in our DFT-optimized structure). This distance is long for a conventional Os−Os bond but is too short to neglect the possibility of interactions between this pair of Os atoms.

The raMO analysis offers an approach to investigate the potential Os−Os bonding at these contacts. Our first step is to consider as a model MO system the 5d, 6s, and 6p orbitals of a single Os atom and see how well this atomic energy level diagram can be reproduced from the basis of the occupied crystal orbitals of Os_3Sn_7 (Figure 6b). Our target eigenfunctions are drawn on the left in the context of the coordination environment of an Os dimer.

After the raMO analysis is performed, the functions drawn on the right of Figure 6b are obtained with non-zero energy eigenvalues. The five 5d orbitals are well reproduced, suggesting that each Os atom has 10 electrons associated with its d orbitals. We will refer to this situation as a $5d^{10}$ configuration, while recognizing that traditional electron counting might formally assign some of these electrons to the surrounding ligand atoms. For the 6s and 6p orbitals the pictures are less clear, as they are more spread out among the surrounding Sn atoms, as might be expected from the high ionization energy of the Os sp orbitals.

A closeup of the function resulting from the p orbital oriented along the Os−Os contact is particularly informative here (Figure 5c). The target Os p orbital (left) appears stabilized by σ-bonding interactions from the surrounding Sn atoms, as well as from a similarly oriented hybrid orbital on the neighboring Os atom. The appearance of an Os−Os bonding interaction in this raMO has profound implications for the electronic structure of the phase. It indicates that the target Os p orbital seldom appears in the wave functions of the system without a bonding contribution from the neighboring Os atom, suggesting the presence of an Os−Os bond.

On the basis of these results, it would seem that the Os atoms might be better treated as dimers rather than individual atoms. In Figure 7, we take this approach, using the MOs for an Os dimer as our target eigenfunctions in the raMO analysis. These eigenfunctions can be naturally grouped according to their symmetry properties into six σ orbitals (Figure 7a), eight π orbitals (Figure 7b), and four δ orbitals (Figure 7c). Within each of these groups, the orbitals are drawn with the bonding combinations at the bottom, nonbonding states near the middle, and antibonding orbitals at the top.

On the left sides of the panels of Figure 7, we show the raMOs corresponding to each of these functions. For the σ orbitals in Figure 7a, most of the target orbitals are well reproduced, with varying degrees of delocalization over the surrounding Sn atoms. The major exception is the sp−sp σ^* orbital (top, left), which shows only vanishing contributions from the Os in its raMO function. The nonoccupation of this σ^* orbital, while its bonding counterpart is well reproduced in the raMOs from the occupied orbitals, is strongly suggestive of net Os−Os bonding.

We should note that this is not an Os−Os bond in the classical two center−two electron sense. The bonding orbital involves supporting interactions from the bridging Sn atoms, making this a multicenter interaction. However, this bonding function exhibits the same nodal properties as a two-center Os−Os σ interaction and may thus be considered as isolobal with a standard Os−Os bond. The balance of transition metal and main group contributions to these interactions could be
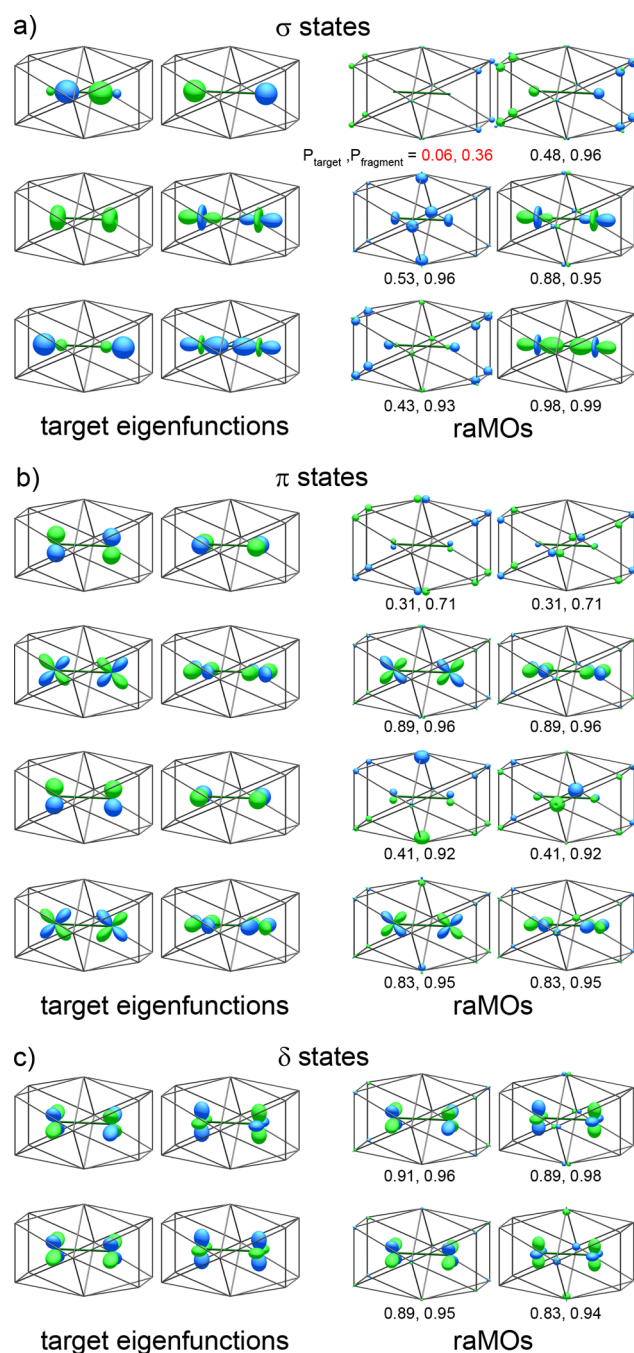

Figure 7. raMOs obtained from the occupied crystal orbitals of Os_3Sn_7, using the molecular orbitals of an Os dimer as target eigenstates: (a) raMOs from targets of Os−Os σ-character; (b) raMOs from targets of π character; (c) raMOs of δ character.

expected to change depending on the relative electronegativities of these elements. This factor may explain why earlier analyses using the electron localization function (ELF) revealed rather variable results from one Ir_3Ge_7-type compound to another.[8]

In Figure 7b, we show the corresponding results for the π type interactions between the Os atoms. Eight target functions result from π or π^* interactions, oriented either parallel or perpendicular to the plane of the page, between either p or d orbitals (with a small amount of admixture between them). The d-based functions are well reproduced in the raMOs, as is consistent with a d^{10} configuration on the Os atoms.

For the p-orbital-based functions, however, much less Os p character is evident in the raMOs. The p−p π^* raMO exhibits very small contributions on the Os_2 pair, which is spread through bonding interactions to the surrounding Sn atoms. The raMO reconstruction of the p−p π bonding target eigenfunction yields larger contributions from the Os_2 pair and its environment, which again are bridged by significant bonding contributions from the bridging Sn atoms. For both, the balance between the Os p and Sn contributions is much more shifted to the Sn, as expected given the lower energies of the Sn s and p orbitals in comparison to the Os p orbitals.

How should these results be interpreted? Equal occupation of the p−p π^* and p−p π bonding functions would result in a net π bond order (which here should be interpreted in an isolobal sense rather than in terms of a localized bond between the Os atoms) of 0. However, it is evident from comparing the raMOs that the bonding function is much better represented in the occupied crystal orbitals than its antibonding counterpart. This would suggest a π-bond order somewhere between 0 and 1 for the interactions both in the plane of the page and perpendicular to the page. As we will see below, the overall electron count for this phase can be well understood by assigning a bond order of 0.5 for each interaction.

The last set of target eignfunctions for the Os_2 dimer are the δ/δ^* orbitals (Figure 7c). All four of these functions are well-reproduced in the raMO analysis, as predicted by the d^{10} configuration of the Os atoms.

From this analysis, we are now in a position to assign a formal electron count to the Os centers of Os_3Sn_7. For isolated Os atoms, we would expect 18 electrons/Os to be the optimal count for fully utilizing the bonding potential of each Os atom's s, p, and d valence orbitals. In this case, however, the Os atoms occur in pairs with functions isolobal with a full Os−Os σ bond and two Os−Os ca. half π bonds. This would suggest that 4 electrons are shared between the Os atoms and that each Os atoms would only need to bring 16 electrons for a closed-shell configuration to be achieved.

If we compare this number to the experimental valence electron count for Os_3Sn_7 of $(3 \times 8 + 7 \times 4)/3 = 17.3$ electrons, it is apparent that there are electrons that are still unaccounted for in our bonding scheme. These electrons can be located by an examination of the remainder raMO functions (with eigenvalues of 0) obtained when the Os_2 dimer MOs are used as target eigenstates. The remainder raMOs (not shown) are focused on the Sn cubes in the fluorite-type fragments, with bonding interactions being apparent at contacts between neighboring cubes along the unit cell diagonal (Figure 8a).

To determine the character of these interactions in more detail, we can perform a raMO analysis on the remainder states obtained during our examination of the Os_2 dumbbells. Here, we consider the Sn−Sn bonding and antibonding functions built from Sn 5s orbitals as target eigenstates (Figure 8b). We then attempt to recover these functions from the remainder raMOs, to see to what extent localized Sn−Sn bonds occur at these contacts.

The resulting Sn-based raMO functions are plotted in Figure 8c. The Sn−Sn bonding raMO appears well localized ($P_{fragment}$ = 0.89, with the remainder of the electron density consisting of tiny contributions scattered throughout the structure). Furthermore, the bonding is enhanced relative to the original target function by s−p hybridization into the contact on both Sn atoms. The form of the raMO then appears to indicate strong Sn−Sn bonding. This conclusion is supported by the
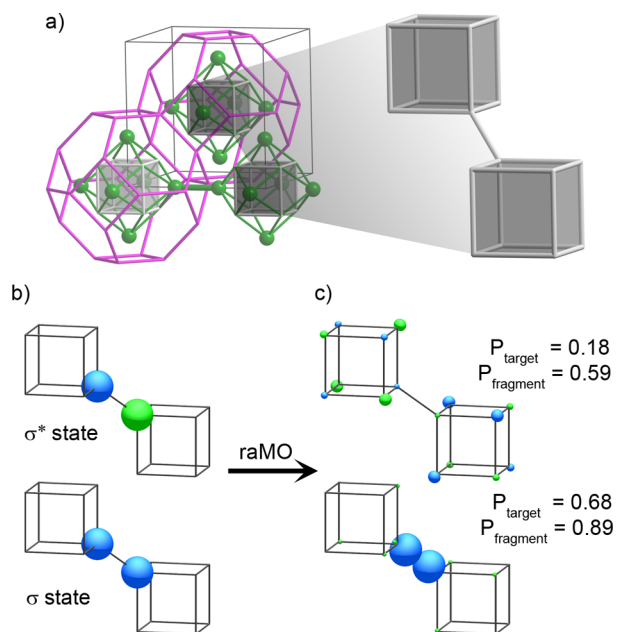

Figure 8. Second iteration of raMO analysis on the remainder functions of Os_3Sn_7 (not contributing to the Os_2 pairs), revealing (a) Sn−Sn bonding between neighboring Sn_8 cubes, (b) target eigenfunctions for σ and σ^* orbitals along one of these Sn−Sn contacts, and (c) the corresponding raMOs generated from the remainder functions.

raMO approximating the Sn−Sn σ^* function: little electron density involving the Sn−Sn contact is apparent here.

Placing a Sn−Sn bond along every bridging contact between the fluorite-type clusters accounts for essentially all of the electron density in the remainder raMOs. With this result in hand, we are now ready to make a full accounting of the valence electrons in Os_3Sn_7. Each Os atom achieves a filled octadecet with 16 electrons, via Os−Os σ and π bonding. Meanwhile, 4 of the 7 Sn atoms in the formula unit lie on the cubes of the fluorite clusters and contribute 1 electron each to Sn−Sn bonding. This leads to a total valence electron count for the bonding scheme of $(16 \times 3 + 4 \times 1)/3 = 17.33$ electrons, in close agreement with the experimental electron count.

6. PROJECTED DOS OF raMO FUNCTIONS

In our calculations thus far, we have worked to map the features of the crystal orbitals of intermetallic phases onto local molecular orbital diagrams. The raMO functions that are created are then fairly localized in space and are orthogonal to each other. This might create the impression that they are essentially noninteracting with each other, but we should remember that they occur in the context of a metallic crystal structure. Some broadening of their energy levels should thus be expected as these are embedded in their structural context, much as the four localized C sp^3/H 1s σ bonds in methane interact to create a_1 and t_2 levels in the full MO diagram.

This broadening of the raMO levels can be tracked using their projected DOS distributions, as is shown in Figure 9. We begin in Figures 9a,b by presenting the full DFT-calibrated Hückel DOS curve for Os_3Sn_7 calculated with a dense k-point grid alongside the corresponding curve obtained from the $2 \times 2 \times 2$ supercell with just the Γ point. As might be expected, the coarse sampling of k space in the latter gives rise to a spikier curve, but the overall distribution and the broad minimum
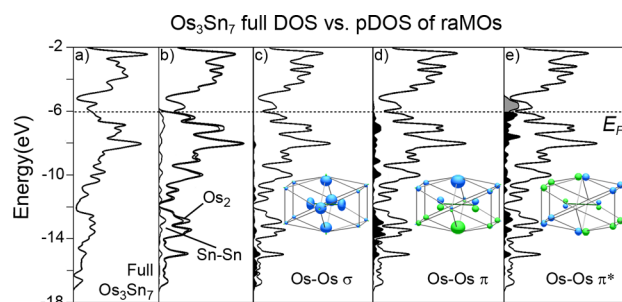
Figure 9. Use of raMO functions in DOS analysis: (a) DFT-calibrated Hückel DOS distribution of Os_3Sn_7; (b) the DOS curve for the Γ point of a $2 \times 2 \times 2$ supercell of Os_3Sn_7, with projections for the Os_2 dimer and Sn−Sn σ raMOs; (c−e) projected DOS distributions for the Os_2 σ, π, and π^* raMOs, respectively. Regions shaded in gray in panels c−e above the E_F correspond to projections from raMOs calculated with the valence electron count changed from 17.33 to 18.33 electrons/Os atom.

around the Fermi energy are well-maintained. The supercell thus provides a fairly representative sampling of the interactions within the structure.

In Figure 9b, we also show projected DOS contributions from the Os_2 dimer and Sn−Sn σ raMOs. Summed together, these account for the full DOS distribution up to the E_F. Above the E_F, their projections are 0, as these raMOs consist of linear combinations of occupied states. The Os_2 DOS dominates the curve throughout, indicating that even the Sn s-rich states at the bottom of the energy scale are deeply involved in bonding with the Os. The Sn−Sn σ raMOs, on the other hand, are spread diffusely over the energy range and have little effect on the total DOS curve's shape.

The different bonding types between the Os atoms have slightly more well-defined energy ranges, as may be seen by an examination of the Os_2 σ, π, and π^* raMOs separately (shaded in black in Figures 9c−e). While the DOS distributions for all three spread across the energy spectrum up to the E_F, the Os_2 σ raMO DOS is particularly concentrated at the lowest end of the DOS distribution, from around −17 to −13 eV. At this point, the Os_2 π appears to take over, until just below the E_F. Near the E_F the π^* functions become dominant. The progression from σ to π to π^* with increasing energy follows the order expected by analogy to molecular systems.

From the DOS curves in Figure 9c−e, it is clear that the orbitals closest to the E_F have a strong π^* character. Removing electrons from the system would thus serve to increase the net π bonding between the transition metal atoms.

How would increasing the electron count affect the bonding? Analyzing this case requires the consideration of unoccupied crystal orbitals. One approach to doing this would be to generate raMOs from the full set of these unoccupied levels and analyze their DOS distributions. We have found, however, that in this case the discontinuities between the raMOs calculated from levels above and below the E_F seriously complicate such an analysis. This issue can be eliminated by probing the states above the E_F in a different way: raising the E_F in the calculation so that more crystal orbitals are included in the analysis. In this way the same raMO functions are used for the projected DOS calculation both above and below the original E_F.

In Figure 9c−e, we have carried out this procedure by including states up across the next DOS peak above the E_F to reach a deep pseudogap at ca. −5.5 eV. Filling the DOS curve to this point corresponds to 18.33 electrons/Os atom, as would

be obtained from replacing each of the Os atoms with Ir to form Ir_3Sn_7. The projected DOS for the Os−Os σ, π, and π^* obtained above the E_F in this way is shaded in gray. A glance at these curves reveals that the DOS peak between the 17.33 and 18.33 electrons/Os atom is predominantly Os−Os π^* in character (the remainder consists of small contributions from a variety of functions). Recalling that the region just below the Os_3Sn_7 E_F also exhibited strong projections onto the Os−Os π^* raMOs, we see that the E_F essentially bisects the Os−Os π^* DOS. Adding electrons to or removing electrons from the system would thus serve to respectively weaken or strengthen the π bonding along these dimer contacts.

In this section, we have seen how the use of raMO functions can be applied in the DOS analysis of intermetallic phases. By calculating the contributions from individual types of raMO functions, such as Os−Os σ, π, and π^*, the advantages of traditional projected DOS and crystal orbital overlap or Hamiltonian population (COOP and COHP)[57−59] analyses can be combined into a single type of plot.

7. raMO ANALYSIS AND ELECTRON COUNT RANGES

Our projected DOS analysis of the Os_3Sn_7 phase indicated that the states just above the E_F are rich in Os−Os π^* character. This observation suggests that, upon increasing the valence electron count through elemental substitution, the additional electrons would serve to weaken the Os−Os π bonding without substantially affecting other interactions in the structure.

This prediction can be tested by applying the raMO analysis to an Ir_3Ge_7-type phase based on a later transition metal element: for example, Ir_3Sn_7. In Figure 10, we present the σ, π,
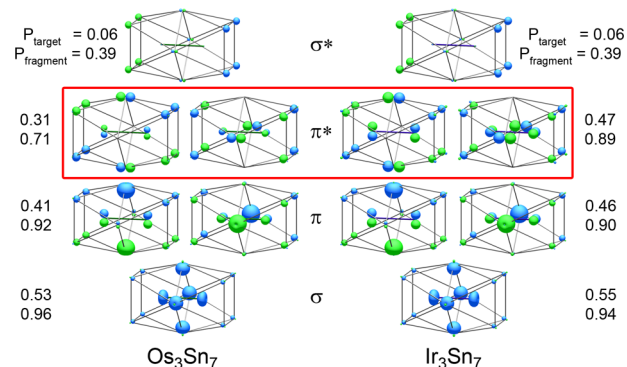

Figure 10. Comparison of the raMOs for the transition metal dimers in the Ir_3Ge_7-type phases Os_3Sn_7 and Ir_3Sn_7. The additional valence electrons introduced into the structure by replacing Os with Ir serve to strengthen the presence of the π^* component to the interactions, leading to no net π bonding.

π^*, and σ^* raMOs for one of the Ir_2 dimers in Ir_3Sn_7 alongside those we obtained earlier for Os_3Sn_7. For the majority of the raMO functions, there is a remarkably close correspondence between the structures. The σ and π functions appear to be essentially unchanged upon substituting Os with Ir. Similarly, the σ^* orbital is poorly represented in both structures, indicating that the σ bonding remains intact in Ir_3Sn_7.

The major change occurs in the π^* raMOs, where the coefficients on the transition metals and bridging Sn atoms grow significantly upon moving from Os_3Sn_7 to Ir_3Sn_7. This effect confirms that the additional electrons are accommodated largely by the π^* functions of the transition metal dimers. For Ir_3Sn_7, this growth in the π^* interactions reaches the point
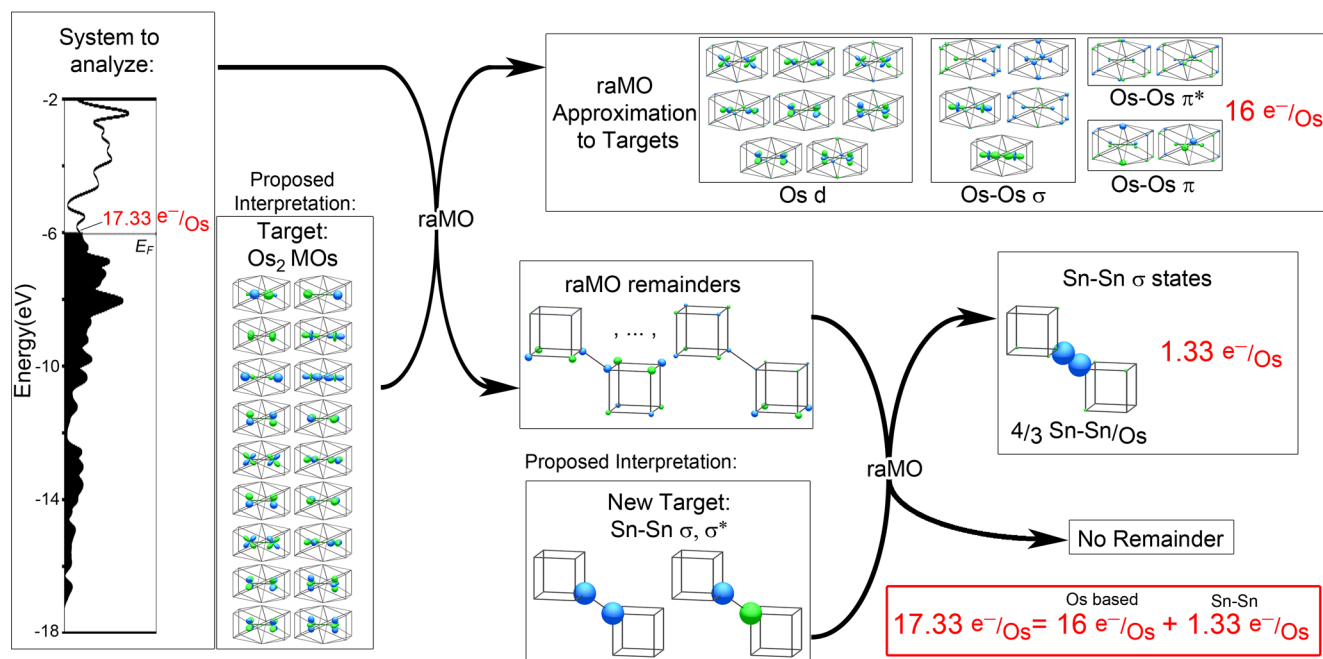
Summary of raMO analysis of Os₃Sn₇

Figure 11. Summary of the use of the raMO analysis to iteratively reduce the full electronic structure of an intermetallic phase into a series of subsystems described by model MO diagrams. For Os_3Sn_7, the result is an explanation of the DOS pseudogap near 17.33 electrons/Os as the sum of Os=Os dimers (16 electrons/Os) and Sn−Sn bonds ($^2/_3$ Sn−Sn bonds/Os = 1.33 electrons/Os).

where it is essentially equal in strength to the stabilizing interactions in the π bonding raMOs. In this phase, then, the π bonding is virtually removed by the occupation of π^* functions, leaving only a σ bond between the Ir atoms. In the absence of π bonding between the Ir atoms, our predicted electron count changes. As the Ir pairs share only a single pair of electrons, they would each require 17 electrons to achieve closed-shell octadecets. This change would lead to an ideal count of $(17 \times 3 + 4 \times 1)/3 = 18.33$ electrons/Ir, which coincides exactly with that calculated from the compound's stoichiometry.

Our identification of a single σ bond to the Ir_2 units of Ir_3Sn_7 provides a somewhat firmer basis for our tentative assignment of double bonds at the corresponding dimers in Os_3Sn_7. Replacing each Ir atom with Os lowers the valence electron count by 1, largely through the depopulation of transition metal−transition metal π^* states. Going from an Ir_2 dimer to an Os_2 dimer would then result in removing two electrons. Pulling these electrons from the π^* states increases the net bond order along the dimers from 1 to 2.

This comparison suggests a mechanism by which transition metal−transition metal bonds can allow 18-electron configurations to be maintained over a range of electron counts. For a pair of atoms joined by a single σ bond, the removal of electrons can be compensated through the sharing of electrons in π bonds. An analogous situation occurs in the molecules F_2, O_2, and N_2, which all follow the octet rule despite having different numbers of valence electrons.

8. CONCLUSIONS

As is so vividly demonstrated by the Zintl−Klemm concept[29] and the orbital interpretations of band structures,[3,25,26] molecular bonding schemes have the potential to bring valuable insights into the structures and properties of solid-state inorganic compounds. In this article, we have presented a

method for rapidly testing and generalizing such molecular ideas: the reverse approximation molecular orbital (raMO) approach. Underlying the raMO approach is the fact that the full wave functions of a system will consist of linear combinations of any localized bonding features that may be present. The localization of these features can be restored through a reversal of the usual basis set approximation of electronic structure calculations: the full wave functions of a compound are considered as being a basis set for the solution of simple molecular orbital problems, such as the interaction between two p orbitals to make a π bond.

We illustrated the raMO method for a series of examples: 1,3-butadiene served as a test case where the bonding is already well understood. Here, the raMO approach quickly yielded a donor−acceptor model for the conjugation of the π system and the orthogonality of this π system to the σ framework of the molecule. Increasingly more complicated compounds, beginning with $CrGa_4$ and then moving to Ir_3Ge_7-type phases, could be similarly dissected into localized bonding systems. For $CrGa_4$, the pseudogap at the E_F was traced to virtually independent 18-electron configurations on each of the Cr atoms. For the Ir_3Ge_7-type phases, a similar pseudogap emerges from 18-electron configurations on the transition metal atoms (facilitated by the covalent sharing of electrons between the transition metals), as well as two center−two electron bonds between main group atoms.

The application to the Ir_3Ge_7-type phase Os_3Sn_7 illustrates how the raMO analysis can be used in an iterative fashion to break down the electronics of complex structures (Figure 11). Beginning with the full electronic structure, we offer a model for the bonding in the form of target eigenfunctions: in this case the MOs of Os_2 dimers. The raMO procedure then yields best approximants to these MOs which amount to 18-electron configurations on the Os atoms achieved with the help of

interactions that are isolobal with Os—Os σ and π bonds. The procedure also yields remainder functions which are orthogonal to the proposed Os_2 dimer based bonding model. A second raMO cycle using a Sn—Sn bonding model can then be applied to these remainder states, which then captures the remaining electron density. At this point, no remainder functions are left, but one could imagine carrying out longer sequences of raMO analysis for more complicated combinations of bonding.

This type of information is complementary to that provided by other theoretical tools for bonding analysis, such as the crystal orbital overlap and Hamiltonian populations (COOP and COHP)[57−59] and the electron localization function and indicator (ELF and ELI).[60−64] The COOP and COHP analyses quantify the bonding strength between pairs of atoms or orbitals in a structure and the dependence of these interactions on electron count. Meanwhile, the ELF and ELI analyze the curvature of the Fermi hole to describe the tendency for electrons to form localized pairs within the structure. New features that are offered by the raMO analysis include the abilities to divide the interactions into orthogonal groups and to partition an integer number of electrons to each of these bonding subsystems. Such a quantization of electron counts in individual bonding systems has historically been a key step in deriving electron-counting rules.

So far, our raMO analyses have been carried out on DFT-calibrated Hückel calculations, which serve as effective atomic orbital based models that quantitatively reproduce the band energies and density of states curves of DFT calculations on the corresponding compounds. However, the formalism is not limited to this particular semiempirical method but in principle could be applied to any first-principles method that employs one-electron wave functions. We are looking forward to developing a DFT implementation of this approach, in which the wave functions in the DFT output are used directly as a basis set for solving simple MO diagrams. In this way, the raMO method should be applicable to the wide range of systems, molecular and periodic, for which DFT provides useful descriptions of electronic structure.

ASSOCIATED CONTENT

Ⓢ Supporting Information

Discussion of the relationship between the raMO and NBO analyses, detailed computational procedures, total energies and DFT-optimized geometries for the intermetallics discussed, and DFT-calibrated Hückel parameters for benzene, $CrGa_4$, Os_3Sn_7, and Ir_3Sn_7. This material is available free of charge via the Internet at http://pubs.acs.org.

AUTHOR INFORMATION

Corresponding Author

*E-mail for D.C.F.: danny@chem.wisc.edu.

Notes

The authors declare no competing financial interest.

ACKNOWLEDGMENTS

REFERENCES

(1) Mott, N. F.; Jones, H. *Theory of the Properties of Metals and Alloys*; Clarendon Press: Oxford, U.K., 1936.

(2) Mizutani, U.; Kondo, Y.; Nishino, Y.; Inukai, M.; Feuerbacher, M.; Sato, H. *J. Phys.: Condens. Matter* **2010**, *22*, 485501.

(3) Berger, R. F.; Walters, P. L.; Lee, S.; Hoffmann, R. *Chem. Rev.* **2011**, *111*, 4522−4545.

(4) Xu, J.-h.; Freeman, A. *Phys. Rev. B* **1989**, *40*, 11927−11930.

(5) Ravindran, P.; Subramoniam, G.; Asokamani, R. *Phys. Rev. B* **1996**, *53*, 1129−1137.

(6) Wolf, W.; Bihlmayer, G.; Blügel, S. *Phys. Rev. B* **1997**, *55*, 6918−6926.

(7) Imai, Y.; Mukaida, M.; Tsunoda, T. *Intermetallics* **2000**, *8*, 381−390.

(8) Häussermann, U.; Elding-Ponten, M.; Svensson, C.; Lidin, S. *Chem. Eur. J.* **1998**, *4*, 1007−1015.

(9) Häussermann, U.; Viklund, P.; Boström, M.; Norrestam, R.; Simak, S. *Phys. Rev. B* **2001**, *63*, 125118-1−125118-10.

(10) Imai, Y.; Watanabe, A. *J. Alloys Compd.* **2006**, *417*, 173−179.

(11) Fredrickson, D. C.; Lee, S.; Hoffmann, R. *Inorg. Chem.* **2004**, *43*, 6159−6167.

(12) Fredrickson, D. C.; Lee, S.; Hoffmann, R.; Lin, J. *Inorg. Chem.* **2004**, *43*, 6151−6158.

(13) Tobola, J.; Pierre, J.; Kaprzyk, S.; Skolozdra, R. V.; Kouacou, M. A. *J. Phys.: Condens. Matter* **1998**, *10*, 1013−1032.

(14) Jung, D.; Koo, H. J.; Whangbo, M. H. *J. Mol. Struct. (THEOCHEM)* **2000**, *527*, 113−119.

(15) Kandpal, H. C.; Felser, C.; Seshadri, R. *J. Phys. D: Appl. Phys.* **2006**, *39*, 776−785.

(16) Kohler, J.; Deng, S. Q.; Lee, C.; Whangbo, M. H. *Inorg. Chem.* **2007**, *46*, 1957−1959.

(17) Fredrickson, R. T.; Fredrickson, D. C. *Inorg. Chem.* **2012**, *51*, 10341−10349.

(18) Fredrickson, R. T.; Fredrickson, D. C. *Inorg. Chem.* **2013**, *52*, 3178−3189.

(19) Han, M. K.; Wu, Y. Q.; Kramer, M.; Vatovez, B.; Grandjean, F.; Long, G. J.; Miller, G. J. *Inorg. Chem.* **2006**, *45*, 10503−10519.

(20) Lin, Q.; Corbett, J. D. *J. Am. Chem. Soc.* **2007**, *129*, 6789−6797.

(21) Berns, V. M.; Stacey, T. E.; Sapiro, M.; Fredrickson, D. C. *Eur. J. Inorg. Chem.* **2011**, *2011*, 3936−3949.

(22) Hadler, A. B.; Fredrickson, D. C. *J. Am. Chem. Soc.* **2012**, *134*, 10361−10364.

(23) Stacey, T. E.; Fredrickson, D. C. *Inorg. Chem.* **2012**, *51*, 4250−4264.

(24) Westbrook, J. H.; Fleischer, R. L. *Magnetic, electrical and optical properties, and applications of intermetallic compounds*; Wiley: Chichester, U.K., and New York, 2000.

(25) Hoffmann, R. *Solids and surfaces: a chemist's view of bonding in extended structures*; VCH: New York, 1988.

(26) Burdett, J. K. *Chemical bonding in solids*; Oxford University Press: New York, 1995.

(27) Zintl, E. *Angew. Chem.* **1939**, *52*, 1−6.

(28) McNeil, M. B.; Pearson, W. B.; Bennett, L. H.; Watson, R. E. *J. Phys. C: Solid State Phys.* **1973**, *6*, 1−10.

(29) Kauzlarich, S. M. *Chemistry, structure, and bonding of Zintl phases and ions*; VCH: New York, 1996.

(30) Klem, M. T.; Vaughey, J. T.; Harp, J. G.; Corbett, J. D. *Inorg. Chem.* **2001**, *40*, 7020−7026.

(31) Li, B.; Corbett, J. D. *Inorg. Chem.* **2002**, *41*, 3944−3949.

2740

dx.doi.org/10.1021/ic4031624 | *Inorg. Chem.* 2014, 53, 2730−2741

(32) Mudring, A.-V.; Corbett, J. D. *J. Am. Chem. Soc.* **2004**, *126*, 5277−5281.

(33) Saparov, B.; Xia, S.-q.; Bobev, S. *Inorg. Chem.* **2008**, *47*, 11237−11244.

(34) Foster, J. M.; Boys, S. F. *Rev. Mod. Phys.* **1960**, *32*, 300−302.

(35) Wannier, G. H. *Phys. Rev.* **1937**, *52*, 191−197.

(36) Marzari, N.; Mostofi, A. A.; Yates, J. R.; Souza, I.; Vanderbilt, D. *Rev. Mod. Phys.* **2012**, *84*, 1419−1475.

(37) Zurek, E.; Jepsen, O.; Andersen, O. K. *ChemPhysChem* **2005**, *6*, 1934−1942.

(38) Shamp, A.; Hooper, J.; Zurek, E. *Inorg. Chem.* **2012**, *51*, 9333−9342.

(39) Hooper, J.; Zurek, E. *Chem. Eur. J.* **2012**, *18*, 5013−5021.

(40) Hoffmann, R. *Angew. Chem., Int. Ed.* **1982**, *21*, 711−724.

(41) Beautiful examples of mapping crystal orbitals onto simple MO diagrams are given by the work of Zurek and co-workers in their analysis of three-center−four-electron bonding in H3- units. See: Shamp, A.; Hooper, J.; Zurek, E. *Inorg. Chem.* **2012**, *51*, 9333−9342. Hooper, J.; Zurek, E. *Chem. Eur. J.* **2012**, *18*, 5013−5021.

(42) Weinhold, F.; Landis, C. R. *Valency and bonding: a natural bond orbital donor-acceptor perspective*; Cambridge University Press: Cambridge, U.K., and New York, 2005.

(43) The technical and prodecural differences between the NBO and raMO analyses are discussed in the Supporting Information.

(44) Cox, E. G. *Rev. Mod. Phys.* **1958**, *30*, 159−162.

(45) Meissner, H.-G.; Schubert, K. *Z. Metallkd.* **1965**, *56*, 523−530.

(46) Künnen, B.; Niepmann, D.; Jeitschko, W. *J. Alloys Compd.* **2000**, *309*, 1−9.

(47) Schlüter, M.; Häussermann, U.; Heying, B.; Pöttgen, R. *J. Solid State Chem.* **2003**, *173*, 418−424.

(48) Kresse, G.; Furthmüller, J. *Phys. Rev. B* **1996**, *54*, 11169−11186.

(49) Kresse, G.; Furthmüller, J. *Comput. Mater. Sci.* **1996**, *6*, 15−50.

(50) Vanderbilt, D. *Phys. Rev. B* **1990**, *41*, 7892−7895.

(51) Stacey, T. E.; Fredrickson, D. C. *Dalton Trans.* **2012**, *41*, 7801−7813.

(52) Landrum, G. A; Glassey, W. *YAeHMOP: Yet Another extended Hückel Molecular Orbital Package, Version 3*; YAeHMOP is freely available at http://sourceforge.net/projects/yaehmop/.

(53) Cohen-Tannoudji, C.; Diu, B.; Laloë, F. *Quantum mechanics*; Wiley: New York, 1977; Vol. *1*, pp 137−138.

(54) Tobola, J.; Pierre, J.; Kaprzyk, S.; Skolozdra, R. V.; Kouacou, M. A. *J. Magn. Magn. Mater.* **1996**, *159*, 192−200.

(55) Tobola, J.; Pierre, J. *J. Alloys Compd.* **2000**, *296*, 243−252.

(56) Pettifor, D. G. *Bonding and structure of molecules and solids*; Oxford University Press: Oxford, U.K., 1995.

(57) Hughbanks, T.; Hoffmann, R. *J. Am. Chem. Soc.* **1983**, *105*, 3528−3537.

(58) Hughbanks, T.; Hoffmann, R. *J. Am. Chem. Soc.* **1983**, *105*, 1150−1162.

(59) Dronskowski, R.; Bloechl, P. E. *J. Phys. Chem.* **1993**, *97*, 8617−8624.

(60) Becke, A. D.; Edgecombe, K. E. *J. Chem. Phys.* **1990**, *92*, 5397−5403.

(61) Savin, A.; Becke, A. D.; Flad, J.; Nesper, R.; Preuss, H.; Von Schnering, H. G. *Angew. Chem., Int. Ed.* **1991**, *39*, 409−412.

(62) Savin, A.; Nesper, R.; Wengert, S.; Fassler, T. F. *Angew. Chem., Int. Ed.* **1997**, *36*, 1808−1832.

(63) Kohout, M.; Pernal, K.; Wagner, F. R.; Grin, Y. *Theor. Chem. Acc.* **2004**, *112*, 453−459.

(64) Wagner, F. R.; Bezugly, V.; Kohout, M.; Grin, Y. *Chem. Eur. J.* **2007**, *13*, 5724−5741.